

Elucidating Na₂KSb band structure: near-band-gap photoemission spectroscopy and DFT calculations

S. A. Rozhkov,^{1,2,*} V. V. Bakin,¹ S. V. Ereemeev,³ V. S. Rusetsky,^{1,4} V. A. Golyashov,^{1,2,5} D. A. Kustov,¹ D. K. Orekhov,^{1,6} H. E. Scheibler,^{1,2,6} V. L. Alperovich,^{1,2} and O. E. Tereshchenko^{1,2,5,†}

¹*Rzhanov Institute of Semiconductor Physics, Siberian Branch,
Russian Academy of Sciences, Novosibirsk 630090, Russia*

²*Novosibirsk State University, Novosibirsk 630090, Russia*

³*Institute of Strength Physics and Materials Science, Russian Academy of Sciences, 634055 Tomsk, Russia*

⁴*JSC "EKARAN FEP", Novosibirsk 630060, Russia*

⁵*Synchrotron Radiation Facility SKIF, Boreskov Institute of Catalysis,
Siberian Branch, Russian Academy of Sciences, Koltsovo 630559, Russia*

⁶*Novosibirsk State Technical University, Novosibirsk 630073, Russia*

(Dated: February 20, 2026)

The electronic band structure of Na₂KSb was studied by a combination of low-energy photoemission spectroscopy and density functional theory (DFT) calculations. The optical and photoemission quantum efficiency (QE) spectra, along with longitudinal energy distribution curves (EDCs) of multialkali Na₂KSb(Cs,Sb) photocathodes were measured in the temperature range of 80–295 K. The thresholds of various band-to-band transition in Na₂KSb were observed in the optical and QE spectra of Na₂KSb(Cs,Sb) photocathodes. The evolution of EDC derivatives with varying photon energy reveals a fine structure related to the emission of two types of electrons: (i) ballistic electrons, which are excited from heavy hole, light hole and split-off valence bands, and (ii) photoelectrons, that are captured in the side valleys of Na₂KSb conduction band. The analysis of EDCs and QE spectra allowed us to determine the band structure parameters of Na₂KSb at $T = 80$ K, including the band gap $E_g = 1.52 \pm 0.02$ eV, spin-orbit splitting $\Delta_{SO} = 0.59 \pm 0.04$ eV and the energy separations between Γ and side valleys of the conduction band: $\Delta_{\Gamma-X_1} = 0.41 \pm 0.05$ eV and $\Delta_{\Gamma-X_2} = 0.65 \pm 0.05$ eV. The experimentally determined band gaps and side valley positions, as well as the energies of the final electronic states of optical transitions are in good agreement with the DFT calculations. The obtained data on the hot electron dynamics and electronic band structure of Na₂KSb are crucial to improve the understanding of the photoemission processes in this material and will contribute to the development of the robust spin-polarized electron sources with multialkali photocathodes.

I. INTRODUCTION

In recent years, the electronic [1–11] and vibrational [12–14] properties of alkali antimonide semiconductor compounds (X_2YSb ; where X and $Y = Li, Na, K, Cs, Rb$) have attracted considerable attention due to their use in the accelerator facilities as electron sources [15–18], as well as in thermoelectric [4, 13, 14] and photovoltaic [10, 19] devices. Electron sources require robust photocathodes with high quantum efficiency (QE) and electron spin polarization, fast response time, as well as low mean transverse energy (MTE), which provides a high brightness. The use of alkali antimonide compounds as photocathodes provides an optimal combination of these key parameters, compared, on the one hand, to robust and fast, but very low-efficient and non-polarized metal photocathodes [20], and, on the other hand, to III-V semiconductor photocathodes with negative effective electron affinity (NEA) [21], which have a record-high QE (up to 0.7) [22] and the ability to generate spin-polarized electrons [23], but a slower response and require extreme-high vacuum for their operation [15, 24].

Among various alkali antimonides, the bialkali cubic Na₂KSb compound with a direct band gap is the most suitable for high-QE (with QE up to 0.1) photocathodes, which are

widely used in near-infrared low-light detection devices and robust high-efficiency electron sources at accelerator facilities [25–27]. The advantage of Na₂KSb is due to the opportunity to activate its surface to the state of NEA by the co-adsorption of Cs and Sb [28–30]. A recent discovery of high spin polarization [31] and low MTE values of electrons emitted from Na₂KSb(Cs,Sb) photocathodes [32, 33] proves the high potential of these photocathodes as robust high-brightness spin-polarized electron sources. As in the case of the III-V semiconductor NEA photocathodes [21, 34], further development and optimization of Na₂KSb(Cs,Sb) photocathodes require the detailed knowledge on the electronic band structure of an active Na₂KSb layer.

The electronic band structure of Na₂KSb was calculated earlier by *ab initio* methods in a number of papers [1, 2, 4, 6, 8, 31, 35]; however, the findings are inconsistent, and only part of them accounted for the spin-orbit interaction [2, 4, 8, 31]. The experimental data on the band structure of Na₂KSb are scarce and also contradictory. So far, the band gap E_g is the only experimentally determined parameter of the Na₂KSb band structure. Moreover, the values of E_g at room temperature $T = 295$ K reported in literature varied from 1.0 eV [28, 36] to 1.4 eV [37, 38]. Recently, the combined experimental studies of optical and photoemission properties of high-efficiency Na₂KSb(Cs,Sb) photocathodes have confirmed the fundamental band gap value $E_g \approx 1.4$ eV at $T = 295$ K [19, 32], as well as the electronic bands order-

* rozhkovs@isp.nsc.ru

† teresh@isp.nsc.ru

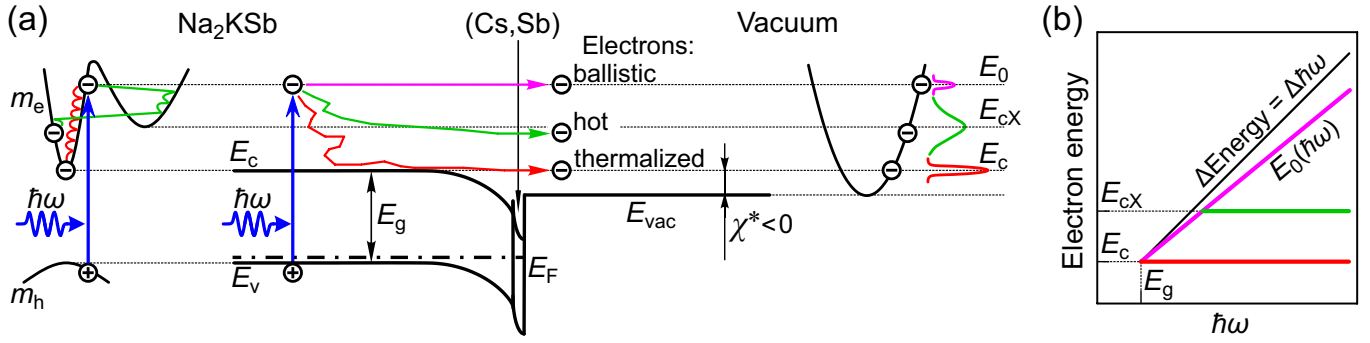


FIG. 1. (a) Schematic energy band diagram of the Na₂KSB(Cs,Sb) photocathode with NEA and the photoemission pathways for ballistic, hot and thermalized electrons. E_c and E_v are the conduction band bottom and the valence band top in Na₂KSB, respectively, E_g is the band gap, E_{vac} is the vacuum level, $\chi^* = E_c - E_{vac}$ is the effective electron affinity, E_F is the Fermi level, E_0 is the energy of ballistic electrons, E_{cX} is the bottom of the conduction band side valley, m_e and m_h are the effective masses of electrons and holes, respectively. (b) The illustration of the dependence of characteristic electron energies on the excitation photon energy $\hbar\omega$.

ing and wave functions symmetry at the center of the Na₂KSB Brillouin zone [31]. Other parameters, such as valence band spin-orbit splitting, effective masses of electrons and holes, side valley positions of the conduction band (CB), which are crucial for the dynamics of non-equilibrium spin-polarized electrons upon photoemission, were not determined experimentally. The main reason for the scarcity of experimental data is the chemical instability of alkali antimonides in the air [39]. Thus, their growth (on foreign substrates) and subsequent studies should be carried out *in situ*, in the same vacuum set-up, ensuring that the samples are not exposed to the air. This hinders the determination of the chemical composition, atomic structure and electronic properties of alkali antimonide films.

The state of NEA on the surface of Na₂KSB(Cs,Sb) photocathodes allows one to explore their near-band-gap photoemission spectroscopy to probe the electronic states in the conduction band of Na₂KSB, as well as the electron dynamics during photoemission [34, 40–44]. The concept of the near-band-gap photoemission spectroscopy relies on the fact that the distribution of hot photoelectrons, which retain a part of their excess energy above thermal energy kT prior to the emission into vacuum, contains a set of features related to the band structure of the photocathode active layer, as illustrated in Fig. 1(a). Indeed, a small fraction of photoelectrons ballistically escape into vacuum without scattering in the active layer. Within the parabolic approximation the initial kinetic energy of photoexcited electrons E_0 in the CB of Na₂KSB equals:

$$E_0(\hbar\omega) = (\hbar\omega - E_g)/(1 + m_e/m_h), \quad (1)$$

where m_e and m_h are the effective masses of electrons and holes, respectively; $\hbar\omega$ is the photon energy. Additionally, hot photoelectrons tend to accumulate in the side valley minima of the CB during thermalization. Therefore, the evolution of the energy distributions of emitted electrons upon varying photon energy should reveal both the thresholds of interband transitions and the CB minima [see Fig. 1(b)].

It should be noted that the accurate measurements of energy and angle distributions of photoelectrons emitted by NEA

photocathodes in the low energy range (< 1 eV) are tricky due to the high sensitivity of low-energy electron trajectories to electric fields produced by a relatively high contact potential difference between NEA photocathodes and other components of electron spectrometers [45–48]. The correct measurements of low-energy electron distributions usually require complex custom-made electron spectrometers [34, 48, 49].

Compact energy electron spectrometers can be realized in vacuum tubes with planar geometry [see Fig. 2(a)]. In such tubes the longitudinal component (E_{lon}) of the total electron kinetic energy (E_k) in vacuum is measured as

$$E_{lon} = E_k \cos^2(\theta) = p_{lon}^2/(2m_0), \quad (2)$$

where θ is the polar emission angle, p_{lon} is the electron momentum component, normal to the photocathode surface, and m_0 is the free electron mass. The electron energy selection is made by applying a uniform retarding electric field between the photocathode and anode. These compact spectrometers proved to be effective in studying the ballistic photoemission from p -GaAs(Cs,O) photocathodes [42, 50, 51], electron energy relaxation by the cascade emission of optical phonons in p -GaN(Cs,O) [44, 52], as well as the energy band diagram and directional photoemission in Na₂KSB(Cs,Sb) photocathodes [19, 31, 32].

The advantages of energy spectroscopy in compact vacuum tubes include the simplicity of apparatus, high energy resolution (~ 1 meV) and high stability of photocathode surfaces (with lifetimes of about 10 years), though they are obtained at the cost of the additional broadening of the measured longitudinal energy distribution curves (EDCs) due to the angular spread of emitted electrons. Since our previous studies indicate that electrons in the multialkali Na₂KSB(Cs,Sb) photocathodes emit predominantly along the normal to the surface [32, 33], the longitudinal energy distributions should closely resemble total kinetic energy distributions.

The studies of the near-band-gap photoemission from p -GaAs(Cs,O) NEA photocathodes proved that electron energy distributions contain a set of features related to the band structure of GaAs, as well as to the mechanisms of electron energy

relaxation and emission into vacuum [34, 42, 53]. These opportunities have not been explored for studying Na₂KSb so far.

It should be noted that the distributions of low energy electrons, emitted from Na₂KSb-based photocathodes, were measured earlier at room temperature in Refs. [54, 55]. However, the fine structure of electron distributions, associated with the photoemission of ballistic electrons, was not observed, and the Na₂KSb band structure parameters were not obtained, apparently, due to the thermal broadening of photoelectron energy distributions [32, 34, 42].

In this work, the electronic band structure of Na₂KSb is studied by a combination of the near-band-gap photoemission spectroscopy of high-efficiency multialkali Na₂KSb(Cs,Sb) NEA photocathodes performed at $T = 80$ K, along with the density functional theory (DFT) calculations of the Na₂KSb electronic band structure. The bulk band gap, spin orbit splitting, side valley positions of the conduction band were obtained from the evolution of energy distributions with varying photon energy. The DFT-calculated energies of the Na₂KSb band structure, along with the energies of the final electronic states of optical transitions, agree well with the experimental values. We also discuss the comparison of the hot electron dynamics and electronic band structures of Na₂KSb and GaAs.

II. EXPERIMENTAL AND COMPUTATIONAL DETAILS

Multialkali Na₂KSb(Cs,Sb) photocathodes were grown on glass substrates [19, 32]. The Na₂KSb film thickness was in the range of 80–140 nm. The Na₂KSb surface was activated to the NEA state by the co-absorption of Cs and Sb. The luminous sensitivities of the produced Na₂KSb(Cs,Sb) films reached up to 850 μ A/lm at $T = 295$ K. The details of the preparation of semitransparent multialkali Na₂KSb(Cs,Sb) photocathodes are presented in Refs. [29, 30]. The compact vacuum photodiodes were fabricated by mounting the planar photocathodes and anodes parallel to each other at a distance of about 0.2 mm on the opposite sides of a cylindrical alumina ceramics body [see Fig. 2(a)]. The working diameter of the photodiodes was equal to 20 mm. The semitransparent anodes were made by depositing 9 nm of Pd on flat glass substrates [56]. The measurements of the transmission, reflection and photoemission QE spectra, as well as the EDCs were performed on Na₂KSb(Cs,Sb) photocathodes in both reflection (R-mode) and transmission (T-mode) illumination geometries. The spectra, measured in the R-mode, were corrected by the anode transmission spectra (with an average transmission of approximately 0.4). The electron longitudinal energy distributions $N_e(E_{\text{lon}})$ were obtained by measuring the derivatives of the photocurrent-voltage characteristics J_{ph} [32, 42]:

$$N_e(E_{\text{lon}}) \sim dJ_{\text{ph}}(U)/dU. \quad (3)$$

The width of an instrumental contour in the EDC measurements was kept at 20% of the energy width of fine features in the EDCs. The measurements were performed in the temperature range of 80–295 K.

The DFT calculations were carried out with the Vienna *ab initio* simulation package (VASP) [57, 58]. For the exchange-correlation potential, the generalized gradient approximation (GGA-PBE) [59] was used to determine the equilibrium structure. The interaction between ion cores and valence electrons was described by the projector augmented-wave method [60, 61], while the alkali metal p orbitals were treated as valence electrons. The Slater-type DFT-1/2 self-energy correction method [62, 63] with a partially ionized antimony potential was applied to obtain the realistic electronic band structure. The spin-orbit coupling (SOC) was taken into account both in the structural relaxation and in the calculation of the electronic band structure.

III. RESULTS

A. Photoemission quantum efficiency spectra of Na₂KSb(Cs,Sb) photocathodes at 80 K

The QE spectra of a Na₂KSb(Cs,Sb) photocathode, measured in both T- and R-illumination geometries at $T = 80$ K, are shown in Fig. 2(c). At low $\hbar\omega$, the QE spectra are characterized by the sharp threshold of interband transitions in Na₂KSb with the band gap E_g of about 1.52 eV [32]. The positions of the threshold are determined by the maxima in the derivatives of the QE spectra. With increasing $\hbar\omega$, QE increases due to the increase in both the light absorption coefficient of the Na₂KSb layer and in the fraction of hot electrons, which emit with a higher escape probability [32]. The second threshold at $\hbar\omega = 2.11$ eV is clearly seen in the R-mode QE spectrum. This threshold is due to the onset of optical transitions from the split-off (SO) valence band to the CB at the photon energy of $E_g + \Delta_{\text{SO}}$, where Δ_{SO} is the spin-orbit splitting. This yields $\Delta_{\text{SO}} = 0.59 \pm 0.04$ eV. The non-monotonous variations of QE in the range of $\hbar\omega \approx 1.6$ –2.3 eV are also caused by the optical interference in the Na₂KSb layer, which partially masks the threshold at $\hbar\omega = E_g + \Delta_{\text{SO}}$ in the T-mode QE spectrum, as is seen in Fig. 2(c). It should be noted that both thresholds at $\hbar\omega = E_g$ and $\hbar\omega = E_g + \Delta_{\text{SO}}$ are clearly seen in the optical transmission spectra of the studied samples (not shown).

Further increase in the photon energy at $\hbar\omega > 2.40$ eV leads to the decrease of the absorption length $\alpha^{-1}(\hbar\omega)$ of Na₂KSb layer to values, significantly smaller than the Na₂KSb layer thickness. In this case, photoelectrons are generated predominantly in the vicinity of the illuminated side of the Na₂KSb layer. For the R-mode illumination, electrons are generated near the emitting surface, which means that they remain in the Na₂KSb layer for only a short time before emission. This results in a reduced thermalization and recombination of electrons and, hence, in a large fraction of hot electrons in the emission current. This leads to the increase of QE with the increasing $\hbar\omega$ [see Fig. 2]. On the contrary, in the case of T-mode illumination, electrons are generated near the glass-Na₂KSb interface, thus, requiring the maximum time to reach the emitting surface. This results in a stronger thermalization and recombination of electrons, and, thus, leads to a decrease

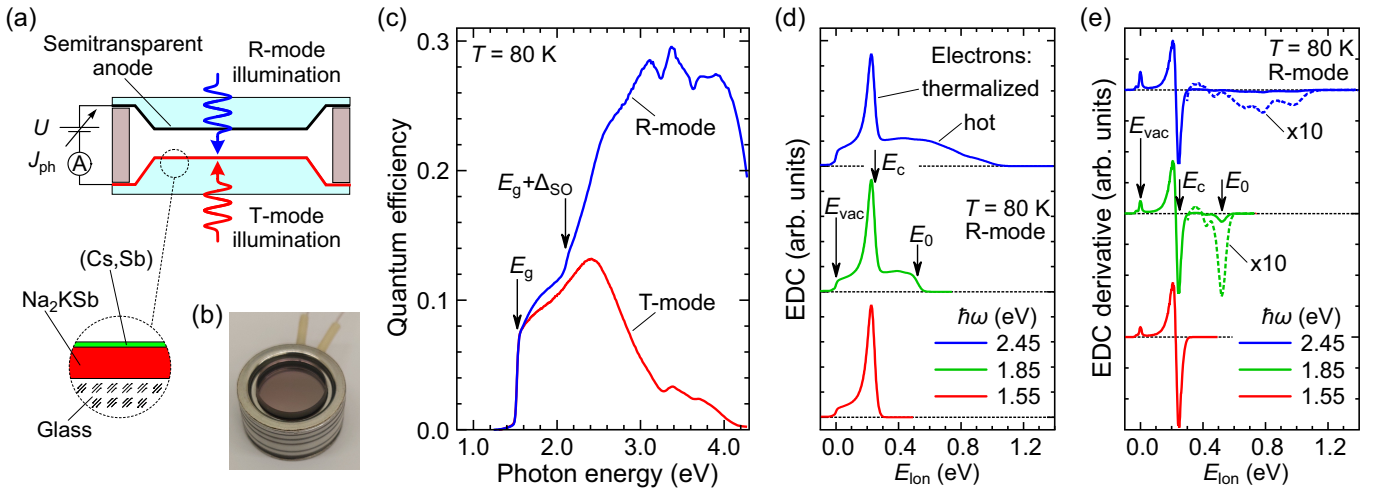


FIG. 2. (a) Schematic cross-section and (b) photograph of a vacuum photodiode with the Na₂KSb(Cs,Sb) photocathode and a semitransparent anode. (c) Photoemission quantum efficiency spectra of the Na₂KSb(Cs,Sb) photocathode measured in transmission (T-mode) and reflection (R-mode) illumination geometries at $T = 80$ K. The threshold energies for transitions from the valence bands to the conduction band (E_g and $E_g + \Delta_{SO}$) are marked with arrows. The R-mode QE spectrum is normalized by the anode transmission spectrum. (d) Typical EDCs and (e) their derivatives of the Na₂KSb(Cs,Sb) photocathode measured in the R-mode at $T = 80$ K. The hot and thermalized electron emission components are indicated for the EDC measured at $\hbar\omega = 2.45$ eV. The vacuum level E_{vac} , conduction band bottom in the bulk of Na₂KSb E_c and the initial kinetic energy of the ballistic electrons in the conduction band E_0 are marked with arrows for EDC and its derivative measured at $\hbar\omega = 1.85$ eV.

in QE at a high $\hbar\omega$. The decrease of the QE above $\hbar\omega \approx 4.0$ eV in both T- and R-mode QE spectra is caused by the optical absorption in the photocathode and anode glass substrates, respectively [see Fig. 2(a)].

As is seen in Fig. 2(c), the QE spectra contain various non-monotonous features in the $\hbar\omega$ range above approximately 2.4 eV. The appearance of these features in both R- and T-mode QE spectra at close photon energies indicates that these features are related to the optical properties of the active Na₂KSb layer of the multialkali photocathode. The measurements of the transmission and reflection spectra showed that these features are caused by the variations of photocathode reflection coefficients, apparently, due to the variations of the optical joint density of states of Na₂KSb [64]. The analysis of these high energy features is beyond the scope of this work and will be presented elsewhere.

B. Photoelectron energy distributions of Na₂KSb(Cs,Sb) photocathodes at 80 K

The longitudinal EDCs of the multialkali Na₂KSb(Cs,Sb) photocathode, measured in the R-mode illumination geometry at $T = 80$ K, are shown in Fig. 2(d). The EDCs are normalized to the maximum values. The EDCs, measured with photon energies exceeding the band gap ($\hbar\omega \geq E_g$), are formed by the emission of thermalized and hot photoelectrons [32]. At low photon energies ($\hbar\omega \approx E_g$) the EDCs are dominated by the emission of thermalized photoelectrons, which lose their excess energy above kT before the emission into vacuum. The thermalized EDC component consists of a narrow peak near the CB bottom E_c and a low-energy wing extend-

ing from E_c down to the vacuum level E_{vac} , which is located about 250 meV below E_c [32]. At a larger $\hbar\omega$, the energy region extending from E_c to the high energy edge of EDC E_0 , is formed by the emission of hot photoelectrons [32]. It is seen in Fig. 2(d) that, with the increasing $\hbar\omega$, the thermalized component of EDC remains almost unchanged, while the hot component extends toward higher energies, and its shape undergoes a complex transformation. It is convenient to study the weak fine structure of EDCs through the analysis of the EDC derivatives (DEDCs) [32, 34, 42], which are shown in Fig. 2(e). Two major stationary (independent of $\hbar\omega$) peaks in DEDC correspond to the vacuum level E_{vac} and the CB bottom in the bulk E_c [32]. The hot component of DEDCs consists of multiple negative peaks with energies and amplitudes depending on $\hbar\omega$.

The evolution of the hot component of EDC derivatives with varying $\hbar\omega$ is shown in Fig. 3. The negative peaks of EDC derivatives can be divided into two groups. The peaks of the first group emerge from the dominating negative peak of the thermalized electrons located near the CB bottom E_c , when $\hbar\omega$ exceeds interband transition thresholds E_g and $(E_g + \Delta_{SO})$. The energy positions of these peaks monotonously increase with the increasing $\hbar\omega$. We labeled these peaks as “HH- Γ_{CB} ”, “LH- Γ_{CB} ” and “SO- Γ_{CB} ” and represented them with a filled square, circle and diamond, respectively, for the EDC derivative measured at $\hbar\omega = 2.45$ eV. The peaks of the second group are stationary and appear at significantly higher photon energies. We labeled these stationary peaks as “X_{CB1}” and “X_{CB2}” and marked them with filled and open triangles, respectively, for the EDC derivatives measured at $\hbar\omega = 2.45$ eV and 3.25 eV. The evolution of the positions of those peaks with varying $\hbar\omega$ is highlighted in Fig. 3 by

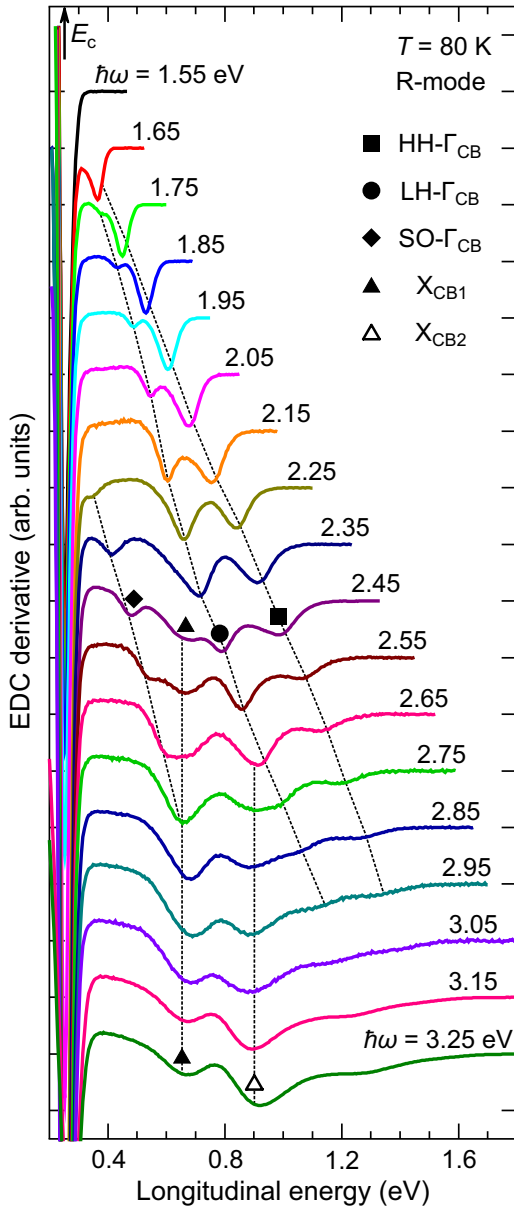


FIG. 3. The evolution of the EDC derivatives of the $\text{Na}_2\text{KSb}(\text{Cs,Sb})$ photocathode with varying $\hbar\omega$ measured in the R-mode at $T = 80$ K. The derivatives are normalized to their maximum absolute values in the hot EDC region of $E_{\text{ion}} > 0.3$ eV (the curves measured at $\hbar\omega = 1.55$ eV and 1.65 eV were normalized by the same value) and shifted vertically for clarity. Negative peaks corresponding to emission of ballistic electrons and hot electrons, scattered to the upper valleys of the conduction band, are marked for $\hbar\omega = 2.45$ eV and $\hbar\omega = 3.25$ eV: $\text{HH-}\Gamma_{\text{CB}}$ (square), $\text{LH-}\Gamma_{\text{CB}}$ (circle), $\text{SO-}\Gamma_{\text{CB}}$ (diamond), X_{CB1} (triangle) and X_{CB2} (open triangle). The evolutions of peak positions with varying $\hbar\omega$ are highlighted with dashed lines as a guides to the eye. The position of the conduction band minima E_c is marked with an arrow.

dashed lines. The peak positions in DEDC as a function of photon energy $\hbar\omega$ are shown in Fig. 4.

First, consider the evolution of $\text{HH-}\Gamma_{\text{CB}}$, $\text{LH-}\Gamma_{\text{CB}}$ and $\text{SO-}\Gamma_{\text{CB}}$ peak energies with varying $\hbar\omega$. At $\hbar\omega$ slightly above E_g

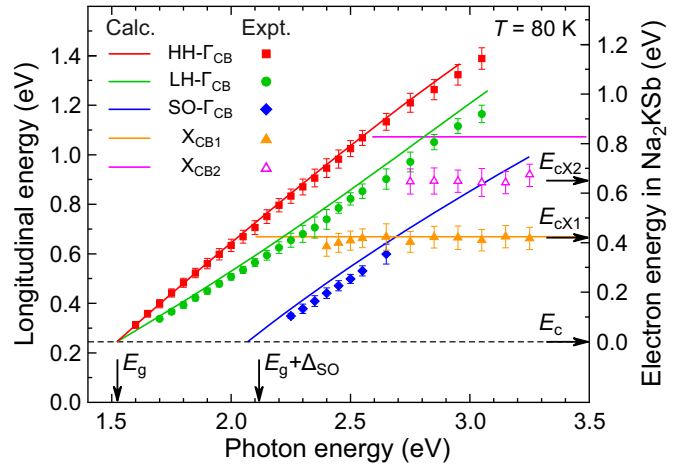


FIG. 4. The evolution of the peak energy positions in EDC derivatives with varying $\hbar\omega$ for the $\text{Na}_2\text{KSb}(\text{Cs,Sb})$ photocathode measured at $T = 80$ K. The DFT-calculated energies of ballistic electrons along the Γ -X direction and the bottoms of the upper valleys of the conduction band are shown with solid lines. The calculated curves are shifted toward the higher $\hbar\omega$ by 0.11 eV to account for the difference between the calculated and measured band gaps (1.41 eV and (1.52 ± 0.02) eV, respectively). The experimentally determined threshold energies of optical transitions from valence bands to the conduction band (E_g and $E_g + \Delta_{\text{SO}}$) and the positions of the conduction band minima (E_c , E_{cX1} and E_{cX2}) are marked with arrows.

(see the curve measured at $\hbar\omega = 1.55$ eV in Fig. 3), the hot electron component is masked by the strong negative peak of thermalized electrons. With the increasing $\hbar\omega$, the $\text{HH-}\Gamma_{\text{CB}}$ and $\text{LH-}\Gamma_{\text{CB}}$ peaks emerge and monotonously move toward higher electron energies. At photon energies $\hbar\omega < 2.0$ eV, both peaks shift approximately proportional to $\hbar\omega$ with slope coefficients $A_{\text{HH}} = 0.83$ and $A_{\text{LH}} = 0.56$ for $\text{HH-}\Gamma_{\text{CB}}$ and $\text{LH-}\Gamma_{\text{CB}}$ peaks, respectively. The emergence of the two peaks just above the band gap of Na_2KSb and the linear dependences of the peak energies on $\hbar\omega$ with slopes lower than unity unambiguously indicate that $\text{HH-}\Gamma_{\text{CB}}$ and $\text{LH-}\Gamma_{\text{CB}}$ peaks correspond to the emission into vacuum of ballistic photoelectrons, which were excited to the CB from the heavy hole (HH) and light hole (LH) valence bands, respectively [34, 42]. As can be seen in Fig. 4, the extrapolated positions of the $\text{HH-}\Gamma_{\text{CB}}$ and $\text{LH-}\Gamma_{\text{CB}}$ peaks at low energies coincide with E_c for $\hbar\omega = E_g$, which indicates that the procedures of determining the band gap value E_g and the position of E_c are valid with an accuracy of about ± 20 meV [32].

Upon a further increase in $\hbar\omega$ the $\text{SO-}\Gamma_{\text{CB}}$ peak emerges near E_c (see the curve measured at $\hbar\omega = 2.25$ eV in Fig. 3). This peak also shifts linearly toward higher energies with the increasing $\hbar\omega$, with the slope coefficient $A_{\text{SO}} = 0.62$. Therefore, the $\text{SO-}\Gamma_{\text{CB}}$ peak is attributed to the emission of the ballistic photoelectrons which were excited to the CB from the SO valence band. As can be seen in Fig. 4, the extrapolation of the $\text{SO-}\Gamma_{\text{CB}}$ peak energy to lower values shows that the $\text{SO-}\Gamma_{\text{CB}}$ peak is located at the bottom of the Na_2KSb CB when $\hbar\omega$ is equal to the second threshold in the QE spectra $E_g + \Delta_{\text{SO}} = 2.11$ eV, which confirms the nature of this spectral

threshold.

Now, consider the stationary X_{CB1} and X_{CB2} peaks. The X_{CB1} peak becomes clearly visible when $\hbar\omega$ reaches approximately 2.4 eV (see EDC derivative measured at $\hbar\omega = 2.45$ eV in Fig. 3), and its position E_{cX1} , which is equal to approximately $E_c + 0.41$ eV, remains unchanged upon a further increase in $\hbar\omega$. A careful examination of the shapes of the EDCs derivatives indicates that the X_{CB1} peak emerges actually at lower $\hbar\omega$. As can be seen in Fig. 4, when $\hbar\omega$ reaches approximately 2.0 eV and, consequently, when the energy of the $HH\text{-}\Gamma_{CB}$ peak reaches E_{cX1} , the ratio of $HH\text{-}\Gamma_{CB}$ peak and $LH\text{-}\Gamma_{CB}$ peak areas abruptly starts to decrease, and these peaks become asymmetric (see curves measured at $\hbar\omega = 2.05$ eV and 2.15 eV in Fig. 3). Apparently, these changes are caused by the emergence of the X_{CB1} peak at $E_{cX1} = E_c + 0.41$ eV.

The X_{CB2} peak evolution is similar to that of the X_{CB1} peak. The X_{CB2} peak position E_{cX2} is equal to approximately $E_c + 0.65$ eV. While it has a well-defined peak shape only at $\hbar\omega > 2.80$ eV (see curve measured at $\hbar\omega = 2.85$ eV in Fig. 3), again, the peak emergence occurs at a lower $\hbar\omega \approx 2.35$ eV (see the curves measured at $\hbar\omega = 2.35\text{--}2.55$ eV in Fig. 3).

The emergence of X_{CB1} and X_{CB2} peaks, along with the changes in the $HH\text{-}\Gamma_{CB}$ and $LH\text{-}\Gamma_{CB}$ peak areas, can be readily explained by the onset of the strong intervalley scattering of the ballistic photoelectrons in the Na_2KSb CB, similarly to GaAs [34, 65, 66]. Thus, we believe that the energies of the stationary X_{CB1} and X_{CB2} peaks correspond to the bottoms of two side valleys of the conduction band at the X point (see below subsection III C); so, the side valley energy positions, with respect to the CB bottom in Na_2KSb $\Delta_{\Gamma-X1}$ and $\Delta_{\Gamma-X2}$, are equal to 0.41 eV and 0.65 eV, respectively.

At $\hbar\omega > 3$ eV we also observed the emergence and evolution of other features in the hot component of the DEDCs. For example, a small negative peak at $E_{lon} \approx 1.3$ eV appears on the curve measured at $\hbar\omega = 3.25$ eV in Fig. 3. Analysis of these high energy features is beyond the scope of the present work.

The evolution of the hot component of EDCs measured in the T-mode illumination geometry (not shown) is very close to that measured in the R-mode for $\hbar\omega < 2.4$ eV. However, at a higher $\hbar\omega$, for the T-mode, the areas of the ballistic $HH\text{-}\Gamma_{CB}$, $LH\text{-}\Gamma_{CB}$ and $SO\text{-}\Gamma_{CB}$ peaks in EDC derivatives rapidly decrease with the increasing $\hbar\omega$ due to the increase in the photon absorption coefficient and, consequently, increase in the mean distance between the region of electron generation and the emitting surface. In particular, the stationary peak X_{CB1} related to the first side valley of CB, is observed in both R- and T-modes. On the contrary, peak X_{CB2} related to the second, higher lying side valley is not observed in the T-mode, presumably, due to a smaller light absorption length at larger photon energies $\hbar\omega > 2.35$ eV.

Upon increasing the photocathode temperature, we observed a thermal broadening and blurring of the fine structure of DEDCs. This highlights the importance of studying the fine structure in DEDCs at cryogenic temperatures. The ballistic peak widths in the EDC derivatives also increase with the increasing $\hbar\omega$. At $T = 80$ K the minimal widths FWHMs (full widths at half maximum) of the ballistic $HH\text{-}\Gamma_{CB}$, $LH\text{-}\Gamma_{CB}$

TABLE I. Measured and calculated energy gaps (in eV) in the Na_2KSb bulk band spectrum.

	E_g	Δ_{SO}	$\Delta_{\Gamma-X1}$	$\Delta_{\Gamma-X2}$
	Experiment			
This work	1.52 ± 0.02	0.59 ± 0.04	0.41 ± 0.05	0.65 ± 0.05
	Calculations			
This work	1.41	0.55	0.42	0.82
DFT-1/2				
GGA [2]	0.51	0.54	0.84	1.07
GGA [8]	0.54	0.55	0.76	1.03
TB-mBJ [4]	1.73	0.47	0.45	0.69
SCAN [8]	1.11	0.54	0.63	0.92
GW [8]	1.51	–	0.77	1.04
(wo-SOC)				

Γ_{CB} and $SO\text{-}\Gamma_{CB}$ peaks at low $\hbar\omega$ are equal to approximately 50 meV and are determined by various physical factors, including possible chemical and doping inhomogeneities of the polycrystalline Na_2KSb layer along with the angular distribution of emitted hot electrons [32]. The quantitative analysis of the evolution of the peaks areas and widths with the increasing electron energy and T is beyond the scope of this work and will be presented elsewhere.

Thus, the measurements of the longitudinal EDCs, along with the optical and QE spectra, allowed us to reveal the details of the hot electron dynamics in Na_2KSb and to determine the band structure parameters of Na_2KSb . The experimentally obtained values of band gap E_g , spin-orbit splitting Δ_{SO} and the intervalley energy separations in the CB $\Delta_{\Gamma-X1}$ and $\Delta_{\Gamma-X2}$ are given in Table I.

C. The DFT-calculated electronic band structure of Na_2KSb

DFT calculations of the electronic structure of Na_2KSb , which took into account spin-orbit interaction, are presented in several papers [2, 4, 8], although these papers are typically focused on the band structure near the Brillouin zone center. In our recent DFT calculation [31], we also focused mainly on the fundamental band gap energy region in order to elucidate the symmetry of the wave functions in Na_2KSb and to explain the experimentally observed photoexcitation of spin-polarized electrons. To describe the experimental results on the band structure and dynamics of hot photoelectrons in Na_2KSb , which are presented in subsections III A and III B, here our calculations are aimed at a more comprehensive numerical evaluation of the Na_2KSb band structure, including the upper lying side valleys of the conduction band, and a realistic evaluation of the effective masses. Our calculations of the bulk spectrum carried out for a primitive unit cell [Fig. 5 (a)] along the high-symmetry directions of the corresponding Brillouin zone [Fig. 5 (b)] are presented in Fig. 5 (c). The notations of the quantities presented in Table I are also provided there. Our calculated energies, alongside with those accurately extracted from the previously published spectra, are compared in Table I. The calculated E_g aligns well with the

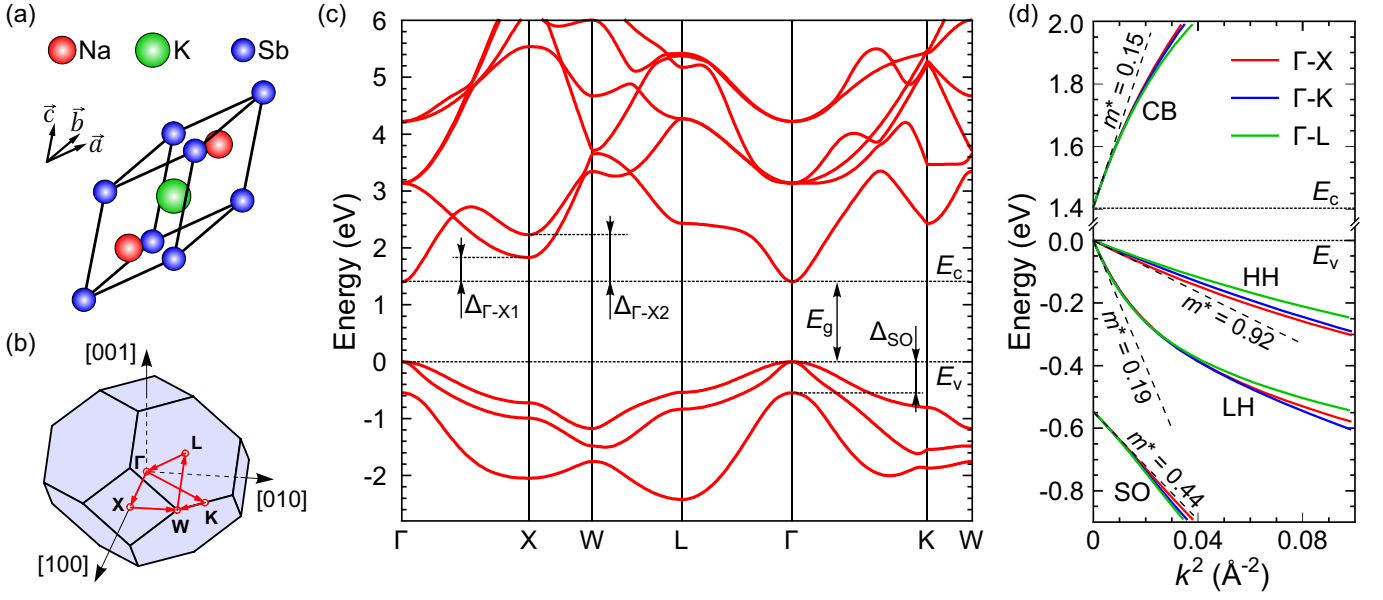


FIG. 5. (a) Balls-and-sticks representation of the primitive cell of cubic Na_2KSb . (b) The Brillouin zone of Na_2KSb . The high-symmetry points and the path connecting them are highlighted. (c) The calculated band structure of Na_2KSb . E_c and E_v are conduction band bottom and valence band top, respectively. The energy gaps (E_g , Δ_{SO} , $\Delta_{\Gamma-X1}$, $\Delta_{\Gamma-X2}$), are highlighted. (d) The calculated band structure of Na_2KSb at the center of the Brillouin zone along Γ -X, Γ -K and Γ -L directions, illustrating the bands non-parabolicity and anisotropy. The parabolic band approximations for the conduction band (CB), heavy hole (HH), light hole (LH) and split-off (SO) valence bands are shown by dashed lines for the Γ -X direction along with respective effective masses (in units of the free electron mass).

experimental value, whereas GGA calculations [2, 8] yield a band gap that is three times smaller than in the measurements. Meta-GGA calculations either overestimate (TB-mBJ [4]) or underestimate (SCAN [8]) the band gap. The GW method [8] shows a perfect numerical agreement with the experimental results; however, these calculations do not account for SOC. At the same time, as can be seen in Table I, the Δ_{SO} values are nearly independent of the calculation method, and our value, obtained in the quasiparticle approach, aligns well with those derived from earlier GGA and meta-GGA calculations, all matching experimental findings closely.

The positions of the stationary peaks X_{CB1} and X_{CB2} in the measured DEDCs, which we believe are responsible for the intervalley scattering of ballistic photoelectrons and are characterized by the energy distances between the bottom of the conduction band at Γ and the side valleys, are in good agreement with the distances to the bottom of two valleys at the X point: $\Delta_{\Gamma-X1}$ and $\Delta_{\Gamma-X2}$ (Fig. 5 (c)). Our calculations for $\Delta_{\Gamma-X1}$ match the experimental value perfectly, while for $\Delta_{\Gamma-X2}$ they show a slight overestimation. Comparing the values of $\Delta_{\Gamma-X1}$ and $\Delta_{\Gamma-X2}$ extracted from earlier calculations with the experimental data, it is evident that only TB-mBJ demonstrates a satisfactory agreement, whereas other methods, including GW , yield significantly larger values, compared to the experiment. Therefore, we can conclude that the bulk spectrum obtained within DFT-1/2 provides the best representation of the experimentally derived band structure, and the assumption that intervalley transitions are determined by unoccupied bands at the X point is validated.

The electron and hole energies of Na_2KSb plotted *versus*

squared wavevector k^2 in the vicinity of the Brillouin zone center are shown in Fig. 5(d) to illustrate the non-parabolicity and anisotropy of the electronic bands. Also, we show the parabolic approximations of the bands in the Γ -X direction by dashed lines with respective effective mass values in units of the free electron mass.

The calculated energies of the conduction band bottoms, as well as the calculated energies of the ballistic electrons, which are excited from the HH, LH and SO valence bands, are shown in Fig. 4 as solid lines. Only the energies of electrons excited along the Γ -X direction are shown since the valence band anisotropy is relatively weak in the energy range of interest.

IV. DISCUSSION

The combination of the near-band-gap optical and photoemission spectroscopy of $\text{Na}_2\text{KSb}(\text{Cs},\text{Sb})$ photocathodes, accompanied by the *ab initio* calculations, revealed that both the hot electron dynamics and electronic band structure of Na_2KSb are qualitatively similar to those of GaAs [34]. As we have already experimentally shown in our previous studies [19, 31, 32], the band gap E_g of Na_2KSb lies in the range of 1.50–1.55 eV at $T = 80$ K, which is close to the band gap of GaAs ($E_g^{\text{GaAs}} = 1.51$ eV).

The obtained value of the Na_2KSb spin-orbit splitting Δ_{SO} of 0.59 eV is by a factor of 2 higher than that of GaAs. This difference is in agreement with a slower reduction of the degree of circular photoluminescence polarization with the increasing $\hbar\omega$ in Na_2KSb , compared to GaAs, as well as

with the high spin-polarization of photoelectrons emitted by Na₂KSb(Cs,Sb) photocathode [31]. Another consequence of a higher Δ_{SO} value in Na₂KSb, compared to GaAs, is that the non-parabolicity of the light hole valence band reveals itself at higher photon energies. As can be seen in Fig. 5(d), the light hole valence band becomes parallel to the HH valence band, when the hole energy reaches $\Delta_{SO}/2$, similar to III-V semiconductors [34].

The evolution of the measured EDCs indicates that the hot electron dynamics in the Na₂KSb CB for electron energies above approximately 0.4 eV is governed by the photoelectron scattering to the side valleys of the Na₂KSb conduction band, similar to GaAs. The examination of the calculated Na₂KSb band structure [see Fig. 5(c)] shows that the two lowest side valleys in the CB are located at the X-point of the Brillouin zone, while in GaAs the first and second side valleys of the CB are located at the L-point and X-point, respectively [34].

It is seen in Fig. 5(c) that another side valley of the Na₂KSb conduction band is located at the K-point of the Brillouin zone. Also, at the L-point there are CB states with a near-horizontal dispersion. Both K-point and L-point features of CB may manifest themselves in the energy distributions of hot electrons. A small negative peak in the EDC derivatives, located at the longitudinal energy of 1.3 eV (see the curve measured at $\hbar\omega = 3.25$ eV in Fig. 3), could be related to one of these features of the Na₂KSb band structure. The analysis of the high energy regions of the band structure is beyond the scope of this work and will be presented elsewhere.

It should be noted that the observation of the EDC features, related to the X-valleys of the conduction band does not necessarily imply that electrons emit into vacuum directly from these X-valleys. Indeed, the direct photoemission from an X-valley could be forbidden due to the electron momentum conservation if the normal to the emitting surface of a Na₂KSb crystallite differs from the $\langle 100 \rangle$ crystallographic direction [21, 34]. In this case, photoelectrons, scattered into an X-valley, may first reenter the Γ -valley before emission. The orientation of the Na₂KSb crystallites in the multialkali photocathodes studied in this work is not exactly known. Previous studies of the Na₂KSb-based photocathodes grown on glass substrates showed that Na₂KSb crystallites are preferentially oriented in the photocathode plane. The predominant crystallographic plane of the Na₂KSb crystallites, parallel to the glass substrate, was reported to be (111) [67] or (210) [68]. The (111) orientation was recently observed also on Na₂KSb grown on a graphene-coated SiC(0001) substrate [69].

As can be seen in Fig. 5(c) and Table I, the DFT-calculated energies of the ballistic electrons in Na₂KSb, as well as side valley energies, are in good agreement with the measured peak energies in the EDC derivatives. The increase in slope in the calculated LH- Γ_{CB} peak energy dependence on $\hbar\omega$ (see Fig. 4), which is located at $\hbar\omega$ of about 2.3 eV, is caused by a strong non-parabolicity of the LH valence band at the hole energies of about $\Delta_{SO}/2$ [see Fig. 5(d)]. This increase in slope is also observed in the experimental data. Small differences between the calculated and measured energies, which are seen for ballistic electrons excited from the LH and SO valence bands (see LH- Γ_{CB} and SO- Γ_{CB} peaks in Fig. 4), may

be caused by the valence band splitting at the Γ -point. This splitting can be induced by a mechanical strain in the Na₂KSb due to the difference in the thermal expansion coefficients of the Na₂KSb polycrystalline film and the glass substrate. Also, it should be noted that the active layer of Na₂KSb(Cs,Sb) photocathode is, in fact, a solid solution Na_{2-x}K_{1+x}Sb [70]; so, the observed differences may be partly caused by small variations of x in the range of 0–0.05.

The dependence of the ballistic electron energy E_0 on $\hbar\omega$ can be used to obtain the ratios of the effective masses of electrons and holes in Na₂KSb, according to the parabolic bands approximation of $E_0(\hbar\omega)$ [see Eq.(1) and Figs. 1(a) and 1(b)]. Using the measured linear slopes A_{HH} , A_{LH} and A_{SO} of the HH- Γ_{CB} , LH- Γ_{CB} and SO- Γ_{CB} peak energy dependences $E_0(\hbar\omega)$, respectively, which were obtained in the electron energy range of 0.1–0.3 eV relative to E_c (see Fig. 4), we determined $m_e/m_{HH} = 0.20 \pm 0.05$, $m_e/m_{LH} = 0.78 \pm 0.11$ and $m_e/m_{SO} = 0.61 \pm 0.09$, where m_e , m_{HH} , m_{LH} and m_{SO} are the effective masses of electrons, heavy holes, light holes and split-off holes in Na₂KSb, respectively. The measured ratios m_e/m_{HH} and m_e/m_{LH} agree, within the experimental error, with the respective calculated effective mass ratios, while the measured ratio m_e/m_{SO} is by a factor of 2 larger than the calculated one [see Fig. 5(d)]. A possible reason for this discrepancy could be the nonlinearity of $E_0(\hbar\omega)$ due to the non-parabolicity of the electron and hole dispersion curves. However, the analysis of the shapes of the calculated $E_0(\hbar\omega)$ curves (see Fig. 4) showed that the variations of linear slopes A_{HH} , A_{LH} and A_{SO} are less than 10% in the energy range of interest; so, the exact reason for the discrepancy between the experimental and calculated m_e/m_{SO} ratios remains unclear.

It is seen in Fig. 3 that, at low photon energies $\hbar\omega < 2.0$ eV, the area of the ballistic HH- Γ_{CB} peak in the DEDCs of the Na₂KSb(Cs,Sb) photocathode exceeds the area of the LH- Γ_{CB} peak by an order of magnitude. On the contrary, in the DEDCs of *p*-GaAs(Cs,O) photocathodes, the areas of these peaks differ only by a factor of 2 [34]. A possible reason for this difference consists in a significantly higher spin-orbit splitting in Na₂KSb and, consequently, later onset of the LH valence band non-parabolicity.

One can assume that various ballistic and stationary peaks, observed in the EDC derivatives of the polycrystalline multialkali Na₂KSb(Cs,Sb) photocathodes, can be related to different chemical phases of the material. Indeed, Na₃Sb, K₃Sb, NaK₂Sb compounds can be formed during the growth of active Na₂KSb layer under nonoptimal conditions [29, 70, 71]. However, these parasitic compounds are *n*-type semiconductors, while Na₂KSb is a *p*-type semiconductor [72]. Consequently, due to the alignment of the Fermi level, the energies of the ballistic electrons in the *n*-type parasitic compounds are by approximately 1 eV lower than in *p*-type Na₂KSb, and, therefore, are not detected in our near-band-gap photoemission experiments. Also, presumably, K₂CsSb and Cs_xSb compounds can be formed at the surfaces of Na₂KSb crystallites during the photocathode activation with Cs and Sb [29, 30, 71, 73]. However, the thicknesses of these activation layers were estimated to be of about 1 nm, which are apparently too small to produce any observable features in the

EDCs and their derivatives for the multialkali photocathodes with active Na₂KSb layer thicknesses of about 100 nm. Again, the photocathodes studied in this work have high luminous sensitivities and QE values near the photoemission threshold E_g , which can be reached only with a high chemical homogeneity of the photocathode active layer and with a large size (about 100 nm) of Na₂KSb crystallites [28, 32, 36]. Finally, the evolution of various peaks in the EDCs derivatives of the Na₂KSb(Cs,Sb) NEA photocathodes with varying $\hbar\omega$ is well explained by the photoelectron excitation and thermalization processes in the homogeneous active layer of the multialkali photocathode.

The elimination of the uncertainties related to the chemical composition and crystallographic orientation of Na₂KSb crystallites requires a successful growth of the monocrystalline or “fiber textured” [74] Na₂KSb films on suitable substrates, along with *ab initio* calculations of the Na₂KSb electronic band structure evolution upon variations in the alkali atom concentrations in a solid solution Na_{2-x}K_{1+x}Sb and upon variations in the mechanical strain in Na₂KSb films.

V. CONCLUSIONS

In summary, we performed the near-band-gap photoemission spectroscopy on the polycrystalline multialkali

Na₂KSb(Cs,Sb) NEA photocathodes, along with the *ab initio* calculations of the Na₂KSb band structure. Our measurements of the energy distribution curves of Na₂KSb(Cs,Sb) photocathodes at various photon energies demonstrated that both the hot electron dynamics and electronic band structure of Na₂KSb exhibit qualitative similarities to those in GaAs. The ratios of the effective masses of electrons and holes, the band gap, spin-orbit splitting and side valley positions of the conduction band of Na₂KSb are obtained from the analysis of energy distributions and photoemission quantum efficiency spectra. The obtained values are in good agreement with the DFT-calculated band structure of Na₂KSb. The obtained results will advance the understanding of photoelectron and spin dynamics in Na₂KSb and will be useful for the development of robust spin-polarized electron sources based on Na₂KSb photocathodes.

ACKNOWLEDGMENTS

The authors acknowledge the support from the Russian Science Foundation (Grant No. 25-62-00004) in the experimental part, SRF SKIF Boreskov Institute of Catalysis (FWUR-2024-0040) and ISP SB RAS. S.V.E. acknowledges the support from the Government research assignment for ISPMS SB RAS, Project No. FWRW-2026-0008.

-
- [1] G. Murtaza, M. Ullah, N. Ullah, M. Rani, M. Muzammil, R. Khenata, S. M. Ramay, and U. Knah, Structural, elastic, electronic and optical properties of bi-alkali antimonides, *Bull. Mater. Sci.* **39**, 1581 (2016).
- [2] S. Yalameha, Z. Nourbakhsh, and A. Vaez, Hydrostatic strain-induced topological phase of KNa₂Sb, *J. Magn. Magn. Mater.* **468**, 279 (2018).
- [3] C. Cocchi, S. Mistry, M. Schmeißer, J. Kühn, and T. Kamps, First-principles many-body study of the electronic and optical properties of CsK₂Sb, a semiconducting material for ultra-bright electron sources, *J. Phys.: Condens. Matter* **31**, 014002 (2019).
- [4] V. K. Sharma, P. C. Sreeparvathy, and V. Kanchana, Na₂KSb: A promising thermoelectric material, *AIP Conf. Proc.* **2115**, 030443 (2019).
- [5] C. Cocchi, S. Mistry, M. Schmeißer, R. Amador, J. Kühn, and T. Kamps, Electronic structure and core electron fingerprints of caesium-based multi-alkali antimonides for ultra-bright electron sources, *Sci. Rep.* **9**, 18279 (2019).
- [6] Z. Khan, G. Murtaza, A. A. Khan, A. Laref, N. A. Kattan, and M. Haneef, Different physical properties of bi-alkali pnictogen compounds using density functional theory, *Int. J. Energy Res.* **45**, 7703 (2021).
- [7] H.-D. Saßnick and C. Cocchi, Electronic structure of cesium-based photocathode materials from density functional theory: performance of PBE, SCAN, and HSE06 functionals, *Electron. Struct.* **3**, 027001 (2021).
- [8] R. Amador, H.-D. Saßnick, and C. Cocchi, Electronic structure and optical properties of Na₂KSb and NaK₂Sb from first-principles many-body theory, *J. Phys.: Condens. Matter* **33**, 365502 (2021).
- [9] X. Wang, K. Zhang, M. Jin, L. Ren, Y. Han, Q. Wang, and Y. Zhang, First-principles investigation of structural, electronic and optical properties of cubic K₂CsSb with different surface orientations, *Solid State Commun.* **356**, 114960 (2022).
- [10] R. Wu and A. M. Ganose, Relativistic electronic structure and photovoltaic performance of K₂CsSb, *J. Mater. Chem. A* **11**, 21636 (2023).
- [11] R. Schier and C. Cocchi, Electronic and optical excitations of K-Sb and Na-Sb crystals, *Phys. Rev. Mater.* **9**, 053804 (2025).
- [12] Q. Zhong, Z. Dai, W. Wang, Y. Zhao, and S. Meng, Quartic anharmonicity and ultra-low lattice thermal conductivity of alkali antimonide compounds M₃Sb (M = K, Rb and Cs), *Int. J. Energy Res.* **45**, 6958 (2021).
- [13] U. Singh, S. Singh, M. Zeeshan, J. van den Brink, and H. Kandpal, Low lattice thermal conductivity in alkali metal based Heusler alloys, *Phys. Rev. Mater.* **6**, 125401 (2022).
- [14] T. Yue, P. Sui, Y. Zhao, J. Ni, S. Meng, and Z. Dai, Theoretical prediction of mechanics, transport, and thermoelectric properties of full Heusler compounds Na₂KSb and X₂CsSb (X = K, Rb), *Phys. Rev. B* **105**, 184304 (2022).
- [15] B. Dunham, J. Barley, A. Bartnik, I. Bazarov, L. Cultrera, J. Dobbins, G. Hoffstaetter, B. Johnson, R. Kaplan, S. Karkare, V. Kostroun, Y. Li, M. Liepe, X. Liu, F. Loehl, J. Maxson, P. Quigley, J. Reilly, D. Rice, D. Sabol, E. Smith, K. Smolenski, M. Tigner, V. Vesherevich, D. Widger, and Z. Zhao, Record high-average current from a high-brightness photoinjector, *Appl. Phys. Lett.* **102**, 034105 (2013).
- [16] P. Musumeci, J. G. Navarro, J. B. Rosenzweig, L. Cultrera, I. Bazarov, J. Maxson, S. Karkare, and H. Padmore, Advances in bright electron sources, *Nucl. Instr. and Meth. A* **907**, 209 (2018).

- [17] I. Petrushina, V. N. Litvinenko, Y. Jing, J. Ma, I. Pinayev, K. Shih, G. Wang, Y. H. Wu, Z. Altinbas, J. C. Brutus, S. Belomestnykh, A. Di Lieto, P. Inacker, J. Jamilkowski, G. Mahler, M. Mapes, T. Miller, G. Narayan, M. Paniccia, T. Roser, F. Severino, J. Skaritka, L. Smart, K. Smith, V. Soria, Y. Than, J. Tuozzolo, E. Wang, B. Xiao, T. Xin, I. Ben-Zvi, C. Boulware, T. Grimm, K. Mihara, D. Kayran, and T. Rao, High-brightness continuous-wave electron beams from superconducting radio-frequency photoemission gun, *Phys. Rev. Lett.* **124**, 244801 (2020).
- [18] L. Guo, K. Shiohara, H. Yamaguchi, G. Wang, Y. Okabe, M. Nakatake, S. Takakura, M. Yamamoto, S. Ogawa, and Y. Takashima, Improved robustness of sequentially deposited potassium cesium antimonide photocathodes achieved by increasing the potassium content towards theoretical stoichiometry, *Sci. Rep.* **15**, 2900 (2025).
- [19] V. S. Rusetsky, V. A. Golyashov, A. V. Mironov, A. Y. Demin, and O. E. Tereshchenko, Photoemission properties of a multi-alkali photocathode, *Optoelectron. Instrum. Data Process.* **57**, 505 (2021).
- [20] D. H. Dowell and J. F. Schmerge, Quantum efficiency and thermal emittance of metal photocathodes, *Phys. Rev. ST Accel. Beams* **12**, 074201 (2009).
- [21] R. L. Bell, *Negative Electron Affinity Devices* (Clarendon Press, Oxford, 1973).
- [22] S. Uchiyama, Y. Takagi, M. Niigaki, H. Kan, and H. Kondoh, GaN-based photocathodes with extremely high quantum efficiency, *Appl. Phys. Lett.* **86**, 103511 (2005).
- [23] D. T. Pierce, F. Meier, and P. Zürcher, Negative electron affinity GaAs: A new source of spinpolarized electrons, *Appl. Phys. Lett.* **86**, 670 (1975).
- [24] N. Chanlek, J. D. Herbert, R. M. Jones, L. B. Jones, K. J. Middleman, and B. L. Milityn, The degradation of quantum efficiency in negative electron affinity GaAs photocathodes under gas exposure, *J. Phys. D: Appl. Phys.* **47**, 055110 (2014).
- [25] L. Cultrera, C. Gulliford, A. Bartnik, H. Lee, and I. Bazarov, Ultra low emittance electron beams from multi-alkali antimonide photocathode operated with infrared light, *Appl. Phys. Lett.* **108**, 134105 (2016).
- [26] F. Zhou, C. Adolphsen, D. Dowell, and R. Xiang, Overview of CW electron guns and LCLS-II RF gun performance, *Front. Phys.* **11**, 1150809 (2023).
- [27] J. Dube, J. Kühn, C. Wang, S. Mistry, G. Klemz, A. Galdi, and T. Kamps, Triple evaporation growth and photoemission characterization of bialkali antimonide photocathodes, *J. Appl. Phys.* **138**, 045704 (2025).
- [28] W. E. Spicer, Photoemissive, photoconductive, and optical absorption studies of alkali-antimony compounds, *Phys. Rev.* **112**, 114 (1958).
- [29] P. Dolizy, Growth of alkali-antimonide films for photocathodes, *Philips Tech. Rev.* **40**, 19 (1982).
- [30] B. Erjavec, Growth and stoichiometry of the Cs_xSb surface film of a high-efficiency, multialkali-antimonide photocathode, *Thin Solid Films* **303**, 4 (1997).
- [31] V. S. Rusetsky, V. A. Golyashov, S. V. Ereemeev, D. A. Kustov, I. P. Rusinov, T. S. Shamirzaev, A. V. Mironov, A. Y. Demin, and O. E. Tereshchenko, New spin-polarized electron source based on alkali antimonide photocathode, *Phys. Rev. Lett.* **129**, 166802 (2022).
- [32] S. A. Rozhkov, V. V. Bakin, V. S. Rusetsky, D. A. Kustov, V. A. Golyashov, A. Y. Demin, H. E. Scheibler, V. L. Alperovich, and O. E. Tereshchenko, $\text{Na}_2\text{KSb}/\text{Cs}_x\text{Sb}$ interface engineering for high-efficiency photocathodes, *Phys. Rev. Appl.* **22**, 024008 (2024).
- [33] S. A. Rozhkov, V. V. Bakin, H. E. Scheibler, V. S. Rusetsky, D. V. Gorshkov, D. A. Kustov, V. A. Golyashov, V. L. Alperovich, and O. E. Tereshchenko, Subthermal mean transverse energies induced by electron refraction on the jump in mass at the surface of multialkali photocathodes (2025), arXiv:2510.02897 [cond-mat.mtrl-sci].
- [34] H.-J. Drouhin, C. Hermann, and G. Lampel, Photoemission from activated gallium arsenide. I. Very-high-resolution energy distribution curves, *Phys. Rev. B* **31**, 3859 (1985).
- [35] A. R. H. F. Ettema and R. A. de Groot, Electronic structure of Na_3Sb and Na_2KSb , *Phys. Rev. B* **61**, 10035 (2000).
- [36] C. Ghosh and B. P. Varma, Preparation and study of properties of a few alkali antimonide photocathodes, *J. Appl. Phys.* **49**, 4549 (1978).
- [37] E.-L. Hoene, Optical and photoelectric properties of multialkali photocathodes, *Adv. Electron. Electron Phys.* **33**, 369 (1972).
- [38] V. P. Beguchev, I. A. Shefova, and A. L. Musatov, Optical and photoemissive properties of multi-alkali photocathodes, *J. Phys. D: Appl. Phys.* **26**, 1499 (1993).
- [39] M. A. H. Schmeißer, S. Mistry, H. Kirschner, S. Schubert, A. Jankowiak, T. Kamps, and J. Kühn, Towards the operation of Cs-K-Sb photocathodes in superconducting rf photoinjectors, *Phys. Rev. Accel. Beams* **21**, 113401 (2018).
- [40] L. W. James and J. L. Moll, Transport properties of GaAs obtained from photoemission measurements, *Phys. Rev.* **183**, 740 (1969).
- [41] J. Peretti, H.-J. Drouhin, D. Paget, and A. Mircéa, Band structure of indium phosphide from near-band-gap photoemission, *Phys. Rev. B* **44**, 7999 (1991).
- [42] D. A. Orlov, V. E. Andreev, and A. S. Terekhov, Elastic and inelastic tunneling of photoelectrons from the dimensional quantization band at a $p^+-\text{GaAs}-(\text{Cs},\text{O})$ interface into vacuum, *JETP Lett.* **71**, 151 (2000).
- [43] M. Piccardo, L. Martinelli, J. Iveland, N. Young, S. P. DenBaars, S. Nakamura, J. S. Speck, C. Weisbuch, and J. Peretti, Determination of the first satellite valley energy in the conduction band of wurtzite GaN by near-band-gap photoemission spectroscopy, *Phys. Rev. B* **89**, 235124 (2014).
- [44] S. A. Rozhkov, V. V. Bakin, D. V. Gorshkov, S. N. Kosolobov, H. E. Scheibler, and A. S. Terekhov, Optical phonon cascade emission by photoelectrons at a $p\text{-GaN}(\text{Cs},\text{O})\text{-vacuum}$ interface, *JETP Lett.* **104**, 135 (2016).
- [45] D. J. Bradley, M. B. Allenson, and B. R. Holeman, The transverse energy of electrons emitted from GaAs photocathodes, *J. Phys. D: Appl. Phys.* **10**, 111 (1977).
- [46] H. Lee, S. Karkare, L. Cultrera, A. Kim, and I. V. Bazarov, Review and demonstration of ultra-low-emittance photocathode measurements, *Rev. Sci. Instrum.* **86**, 073309 (2015).
- [47] F. Ichihashi, X. Dong, A. Inoue, T. Kawaguchi, M. Kuwahara, T. Ito, S. Harada, M. Tagawa, and T. Ujihara, Development of angle-resolved spectroscopy system of electrons emitted from a surface with negative electron affinity state, *Rev. Sci. Instrum.* **89**, 073103 (2018).
- [48] S. Karkare, J. Feng, J. Maxson, and H. A. Padmore, Development of a 3-D energy-momentum analyzer for meV-scale energy electrons, *Rev. Sci. Instrum.* **90**, 053902 (2019).
- [49] D. A. Orlov, M. Hoppe, U. Weigel, D. Schwalm, A. S. Terekhov, and A. Wolf, Energy distributions of electrons emitted from GaAs(Cs,O), *Appl. Phys. Lett.* **78**, 2721 (2001).
- [50] V. V. Bakin, A. A. Pakhnevich, S. N. Kosolobov, H. E. Scheibler, A. S. Jaroshevich, and A. S. Terekhov, Refraction of thermalized electrons emitted ballistically into vacuum from $p^+-\text{GaAs}-(\text{Cs},\text{O})$, *JETP Lett.* **77**, 167 (2003).

- [51] O. E. Tereshchenko, V. A. Golyashov, A. A. Rodionov, I. B. Chistokhin, N. V. Kislykh, A. V. Mironov, and V. V. Aksenov, Solar energy converters based on multi-junction photoemission solar cells, *Sci. Rep.* **7**, 16154 (2017).
- [52] A. A. Pakhnevich, V. V. Bakin, A. V. Yaz'kov, H. E. Scheibler, S. V. Shevelev, O. E. Tereshchenko, A. S. Yaroshevich, and A. S. Terekhov, Energy distributions of photoelectrons emitted from p -GaN(Cs,O) with effective negative electron affinity, *JETP Lett.* **79**, 479 (2004).
- [53] A. S. Terekhov and D. A. Orlov, Fine structure in the spectra of thermalized photoelectrons emitted from GaAs with negative electron affinity, *JETP Lett.* **59**, 864 (1994).
- [54] C. Ghosh, Photoemission and optical processes in multialkali photocathodes, *Phys. Rev. B* **22**, 1972 (1980).
- [55] V. P. Begucheve, I. A. Shefova, and M. N. Shulgina, Investigation of photoelectron distribution by energies from the multialkali photocathode Na_2KSbCsO , *Zhurnal Tekhnicheskoi Fiziki* **58**, 1594 (1988).
- [56] O. E. Tereshchenko, V. V. Bakin, S. A. Stepanov, V. A. Golyashov, A. S. Mikaeva, D. A. Kustov, V. S. Rusetsky, S. A. Rozhkov, H. E. Scheibler, and A. Y. Demin, Direct spin-imaging detector based on freestanding magnetic nanomembranes, *Phys. Rev. Lett.* **134**, 157002 (2025).
- [57] G. Kresse and J. Hafner, *Ab initio* molecular dynamics for open-shell transition metals, *Phys. Rev. B* **48**, 13115 (1993).
- [58] G. Kresse and J. Furthmüller, Efficient iterative schemes for *ab initio* total-energy calculations using a plane-wave basis set, *Phys. Rev. B* **54**, 11169 (1996).
- [59] J. P. Perdew, K. Burke, and M. Ernzerhof, Generalized gradient approximation made simple, *Phys. Rev. Lett.* **77**, 3865 (1996).
- [60] P. E. Blöchl, Projector augmented-wave method, *Phys. Rev. B* **50**, 17953 (1994).
- [61] G. Kresse and D. Joubert, From ultrasoft pseudopotentials to the projector augmented-wave method, *Phys. Rev. B* **59**, 1758 (1999).
- [62] L. G. Ferreira, M. Marques, and L. K. Teles, Approximation to density functional theory for the calculation of band gaps of semiconductors, *Phys. Rev. B* **78**, 125116 (2008).
- [63] L. G. Ferreira, M. Marques, and L. K. Teles, Slater half-occupation technique revisited: the LDA-1/2 and GGA-1/2 approaches for atomic ionization energies and band gaps in semiconductors, *AIP Advances* **1**, 032119 (2011).
- [64] S. H. Rhim, M. Kim, A. J. Freeman, and R. Asahi, Fully first-principles screened-exchange LDA calculations of excited states and optical properties of III-V semiconductors, *Phys. Rev. B* **71**, 045202 (2005).
- [65] G. Fasol, W. Hackenberg, H. P. Hughes, K. Ploog, E. Bauser, and H. Kano, Continuous-wave spectroscopy of femtosecond carrier scattering in GaAs, *Phys. Rev. B* **41**, 1461 (1990).
- [66] J. Kanasaki, H. Tanimura, and K. Tanimura, Imaging energy-, momentum-, and time-resolved distributions of photoinjected hot electrons in GaAs, *Phys. Rev. Lett.* **113**, 237401 (2014).
- [67] P. Dolizy, F. Grolière, and M. Lemonier, High performance with trialkaline antimonide photocathodes, *Adv. Electron. Electron Phys.* **74**, 331 (1988).
- [68] T. Ninomiya, K. Taketoshi, and H. Tachiya, Crystal structure of multialkali photocathodes, *Adv. Electron. Electron Phys.* **28**, 337 (1969).
- [69] N. Y. Solovova, V. A. Golyashov, S. V. Ereemeev, S. Y. Priobrazhenskii, S. P. Lebedev, A. A. Lebedev, V. S. Rusetsky, and O. E. Tereshchenko, Revealing the (111) surface electronic structure of epitaxially grown Na_2KSb photocathode (2026), arXiv:2601.19652 [cond-mat.mtrl-sci].
- [70] W. McCarroll, Phases in the photoelectric sodium-potassium antimony system, *J. Phys. Chem. Solids* **16**, 30 (1960).
- [71] A. A. Dowman, T. H. Jones, and A. H. Beck, Scanning electron diffraction studies on alkali antimonide photocathodes, including the S20, *J. Phys. D: Appl. Phys.* **8**, 69 (1975).
- [72] W. H. McCarroll, R. J. Paff, and A. H. Sommer, Role of Cs in the (Cs) Na_2KSb (S-20) multialkali photocathode, *J. Appl. Phys.* **42**, 569 (1971).
- [73] L. Galan and C. W. Bates Jr, Structure of multialkali antimonide photocathodes studied by x-ray photoelectron spectroscopy, *J. Phys. D: Appl. Phys.* **14**, 293 (1981).
- [74] C. T. Parzyck, C. A. Pennington, W. J. I. DeBenedetti, J. Balajka, E. M. Echeverria, H. Paik, L. Moreschini, B. D. Faeth, C. Hu, J. K. Nangoi, V. Anil, T. A. Arias, M. A. Hines, D. G. Schlom, A. Galdi, K. M. Shen, and J. M. Maxson, Atomically smooth films of CsSb: A chemically robust visible light photocathode, *APL Mater.* **11**, 101125 (2023).